

Dynamic Clutter Mitigation Using Sparse Optimization

Faruk Uysal
C&P Technologies Inc.

Ivan Selesnick
New York University Polytechnic School of Engineering

Unnikrishna Pillai
C&P Technologies Inc. and New York University Polytechnic School of Engineering

Braham Himed
Sensors Directorate, Air Force Research Laboratory

INTRODUCTION

The impact of wind farms on radar systems, such as air traffic control (ATC), air defense (AD), and weather radars, is a significant issue, especially considering that demand for wind power and wind farms is increasing dramatically. According to the American Wind Energy Association, more than 51,630 MW of wind power capacity are installed in the United States [1]. There are also more than 8,900 MW of wind power capacity under construction, involving more than 90 separate projects spanning 31 states and Puerto Rico [2].

Wind farms have up to several hundred wind turbines with blades up to 100 ft in length. The size and rotation of these blades present technical challenges to the effectiveness of ATC, AD, and weather radar systems. Several studies have documented the adverse effect of wind turbines and wind farms on radar returns (echoes) [3], [4], [5]. The Doppler shift because of the rotating blades may share many characteristics with small targets, which causes false alarms. Echoes from targets may be masked by radar returns created by the rotating wind turbine blades or wind turbine towers. Wind turbine blades may obstruct the radars' coverage view [6]. These effects are known as masking and shadowing, re-

spectively. Wind turbine clutter may cause track reduction and a rise in the detection thresholds in AD radars. Wind turbine clutter has not had a major negative impact on forecast operations; however, misidentification of thunderstorm features, false estimates of precipitation accumulation, and incorrect storm identification and tracking have been reported near large wind turbine installations [7]. Thus, methods to mitigate wind turbine clutter effects are becoming important to maintain the national airspace system and national weather service capabilities.

Planning wind farm locations to minimize possible disturbances to local radar and communications systems is possible. However, this method is not applicable for installed systems. Possible solutions have been proposed to mitigate wind turbine clutter effects, including the development of radar-friendly low radar cross-section (RCS) turbines and turbine blades using stealth technology. However, this method is expensive and may degrade the efficiency of the lightning protection of turbines [8]. Mitigation of wind turbine clutter by advanced signal processing techniques is more practical and may involve minor modification of installed hardware systems.

This article explores the use of sparse-optimization techniques to separate dynamic wind turbine clutter from terrain or topographical features (static clutter) and moving targets. It is assumed that moving targets and dynamic clutter (produced by wind turbines) can be distinguished by the degree to which their Doppler spectra vary with time. Because of the rotation of their blades, wind turbines are seen to produce radar returns with strongly time-varying Doppler spectra. It is further assumed that constant-velocity targets exhibit stationary (or slow-varying) Doppler spectra (relative to that of wind turbines). We aim to express the radar IQ data as the explicit sum of two such "morphologically" distinct components, and we apply morphological component analysis (MCA) [9] to achieve their separation. MCA is applicable only when the two components admit sparse

Authors' current addresses: F. Uysal, U. Pillai, C&P Technologies Inc., 317 Harrington Ave., Suite 9, Closter, NJ 07624 USA. I. Selesnick, U. Pillai, New York University Polytechnic School of Engineering, Brooklyn, NY 11201 USA. B. Himed, AFRL/RVMD, Dayton, OH 45433 USA.

The views expressed are those of the author and do not reflect the official policy or position of the Department of Defense or the U.S. Government. Distribution Statement A (Approved for Public Release, Distribution Unlimited).

Manuscript SYSAES-2013-0137 received August 19, 2013, revised February 20, 2014, and ready for publication March 26, 2014.

DOI: 10.1109/MAES.2014.130137.

Review handled by K. Kulpa.

0885/8985/14 \$26.00 © 2014 IEEE

representations with respect to distinct transforms. To this end, we model radar returns produced by moving targets as sparse with respect to the Fourier transform (FT), assuming targets are moving at a constant velocity during the coherent processing interval (CPI). Because of the time-varying Doppler characteristics of rotating blades, we model radar returns produced by wind turbines as sparse with respect to the short-time Fourier transform (STFT), where the STFT window is chosen appropriately.

This article more generally considers the problem of separating radar returns into distinct components based on distinguishing time-varying Doppler characteristics, even when the components overlap in time, frequency, and time-frequency. To illustrate the generality of the MCA approach for this purpose, we also illustrate its use to suppress transient interference, which causes Doppler streaking in range-Doppler profile images [10].

MODELING WIND TURBINE CLUTTER

The time-domain and Doppler signatures of rotating objects have been well studied, and numerous approaches have been proposed to define suitable mathematical models [11], [12], [13]. In this article, we assume the time-domain signa-

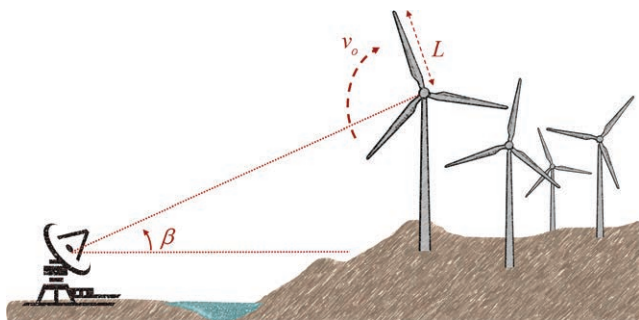


Figure 1.
Radar and wind turbines.

ture of wind turbine clutter follows the simplified mathematical model of rotating blades given in [12, Sec. 3.2.1]. Although more sophisticated modeling is required to represent the real-life wind farms shown in Figure 1, the following approach helps to illustrate the time-varying Doppler present in the wind turbine clutter returns.

For a set of B blades, which are rotating with angular velocity v_o , have a length of L , and are at elevation angle β with respect to the radar line of sight (for simplicity, the azimuth angle is assumed to be zero), the total radar return is modeled by

$$s_{\text{wtc}}(t) = A \sum_{k=1}^B \text{sinc} \Omega_k(t) e^{-j(\Omega_k(t) + \omega_o t)} \quad (1)$$

for a typical transmit waveform centered at frequency ω_o and

$$\Omega_k(t) = \frac{2\pi L f_o}{c} \cos \beta \cos \left(v_o t + \frac{k 2\pi}{B} \right) \quad (2)$$

Expanding (1) in terms of Bessel functions shows that the spectrum of a scatterer on the turning blades consists of multiple spectral lines around the center frequency, with a spacing of $v_o/2\pi$ between adjacent lines [11]. However, because of the various aspect angles generated at the multiple scattering centers situated along each blade, this results in a continuous distribution for the wind turbine spectrum, as shown in Figure 2a. Consequently, returns from wind turbines cannot be sparsely represented using the FT.

We use the preceding mathematical model to simulate a wind turbine with three blades, which are rotating with an angular velocity of $v_o = 12$ rpm, have a blade length of $L = 60$ m, are at an elevation angle $\beta = 45^\circ$ with respect to the radar line of sight, and are at a range of 707 m. The simulated turbine's power spectral density is shown in Figure 2a. Other simulation parameters are chosen similar to an S-band side-looking stationary radar with a pulse repetition frequency of 3 kHz.

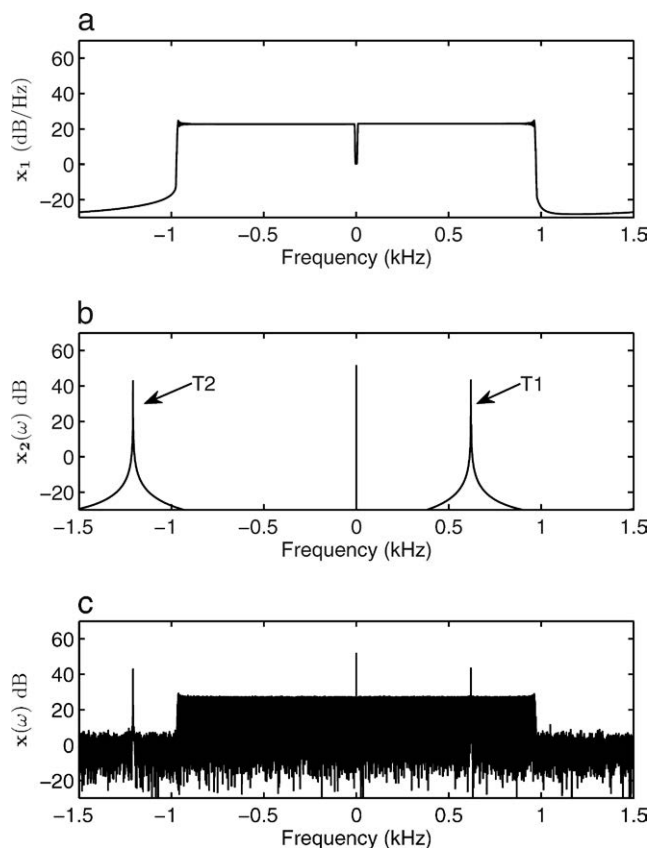


Figure 2.

(a) Power spectral density of simulated wind turbine clutter. (b) Frequency spectrum of simulated targets and stationary ground clutter. (c) Frequency spectrum of simulated radar return, including targets, stationary ground clutter, wind turbine clutter, and noise.

We simulate moving targets using a narrowband signal model, assuming ideal scatterers, as described in [14]:

$$s_{\text{tar}}(t) = e^{-j2\pi f_0 2(R_{\text{tar}} + v_{\text{tar}}t) \cos \theta / c}, \quad (3)$$

where R_{tar} is the target range, θ is the target angle, and v_{tar} is the target velocity. As seen from (3), returns from the moving target can be sparsely represented in the frequency domain. Figure 2b shows the frequency spectrum of the simulated radar return that comprises two moving targets, T1 and T2, with constant Doppler frequencies (0.6 and -1.2 kHz, respectively) and stationary ground clutter (0 Hz). As seen in Figure 2b, constant-velocity targets and stationary clutter can be represented sparsely in the frequency domain.

Figure 2c shows the total simulated radar return $s(t)$ comprising two moving targets, stationary ground clutter, rotating blades (to mimic wind turbine clutter), and noise:

$$s(t) = s_{\text{tar}}(t) + s_{\text{wtc}}(t) + w(t). \quad (4)$$

In the simulation, the noise power is set as 0 dB. For each target, the target-to-noise ratio is 5 dB. The ground clutter-to-noise ratio is 20 dB, and the wind turbine clutter-to-noise ratio is 40 dB. In the simulation, we have set the velocity of

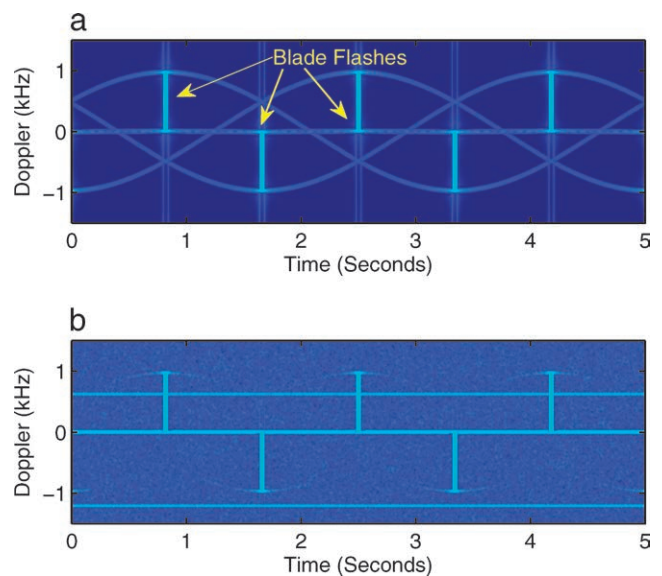


Figure 3.

(a) Spectrogram of wind turbine radar returns for 5 s. (b) Spectrogram of the simulated radar return, including targets, stationary ground clutter, wind turbine clutter, and noise.

target T1 (shown in Figure 2b at 0.6 kHz) so that its Doppler frequency is within the wind turbine clutter spectrum, as shown in Figure 2c. It is possible to separate target T2 (shown in Figure 2b at -1.2 kHz) from the wind turbine clutter by conventional frequency filtering. However, because target T1 is buried in the wind turbine clutter, it cannot be separated by frequency filtering.

As noted earlier, assuming the targets have a constant velocity during the CPI, the radar returns they produce can be sparsely represented in the frequency domain using the FT. In contrast, the radar returns produced by the rotating blades have a continuous distribution in the frequency domain. The radar echoes from the rotating blades (i.e. wind turbine clutter) produce time-varying Doppler signatures; hence, they are more sparsely represented in the time-frequency domain using the STFT than in the frequency domain using the FT. Unlike the FT, the STFT is suitable for nonstationary signals comprising time-varying frequency components.

Time-frequency analysis of the simulated wind turbine radar returns for one full rotation of turbine blades (i.e., 5 s) is shown in Figure 3a using the STFT. In contrast to the non-sparse frequency domain representation shown in Figure 2a, (idealized) wind turbine clutter can be sparsely represented in the time-frequency domain. The returns from the rotating blades generate strong periodic “flashes” because of the high RCS when the face of the blade is directed to the radar. These flashes are visible in the spectrogram as vertical lines in Figure 3a. Energy along the horizontal line at the direct zero frequency is because of returns from the body of the wind turbine.

As an alternative representation to Figure 2c, Figure 3b shows the time-frequency representation of the total radar return for a 5-s interval. By taking advantage of time-fre-

quency analysis, it is possible to mostly separate targets T1 and T2 from the wind turbine clutter by applying conventional band-pass filters ~ 0.6 and ~ 1.2 kHz. However, this method is only applicable if the target moves with a constant velocity in the given CPI.

From the total signal $s(t)$ in (4), we aim to recover components $s_{\text{tar}}(t)$ and $s_{\text{wtc}}(t)$ individually. The MCA separation approach method relies on each of s_{tar} and s_{wtc} having a sparse representation; otherwise, it is not applicable. Moreover, the domains must be incoherent (i.e., contain features with different morphologies that are sparse in their respective representations [15]) to recover s_{tar} and s_{wtc} from radar returns s . Returns from moving targets s_{tar} can be sparsely represented using the FT domain, provided that they can be assumed to be moving at constant velocity during the CPI. However, radar echoes produced by wind turbine clutter, s_{wtc} , which constitute a time-varying Doppler component, are more sparsely represented by using the STFT than by using the FT.

SIGNAL SEPARATION

To suppress wind turbine clutter in radar returns, we consider the explicit representation of the radar return as a sum of the two components. For that purpose, we consider the generic problem where an observed signal, $\mathbf{x} \in \mathbb{C}^N$, is to be modeled as the sum of two components signals, \mathbf{x}_1 and \mathbf{x}_2 :

$$\mathbf{x} = \mathbf{x}_1 + \mathbf{x}_2. \quad (5)$$

The recovery of \mathbf{x}_i from \mathbf{x} is ill conditioned: there are infinite solutions. One may set \mathbf{x}_1 arbitrarily and set $\mathbf{x}_2 = \mathbf{x} - \mathbf{x}_1$. Hence, the estimation of \mathbf{x}_i from \mathbf{x} can be meaningfully performed only when (1) they have distinct properties and (2) these properties are known or approximately known.

In this article, we use the MCA approach, which assumes only that the signals of the two components \mathbf{x}_1 and \mathbf{x}_2 admit sparse representations with respect to distinct transforms \mathbf{F}_1 and \mathbf{F}_2 , respectively [9]. One formulation of MCA aims to find coefficients \mathbf{a}_i with respect to transforms \mathbf{F}_i . In this formulation, the component signals are represented (synthesized) in terms of the coefficients, as¹

$$\mathbf{x}_1 = \mathbf{F}_1 \mathbf{a}_1, \quad \mathbf{x}_2 = \mathbf{F}_2 \mathbf{a}_2. \quad (6)$$

Therefore, instead of finding \mathbf{x}_1 and \mathbf{x}_2 such that $\mathbf{x} = \mathbf{x}_1 + \mathbf{x}_2$, this formulation of MCA seeks \mathbf{a}_1 and \mathbf{a}_2 such that

$$\mathbf{x} = \mathbf{F}_1 \mathbf{a}_1 + \mathbf{F}_2 \mathbf{a}_2. \quad (7)$$

This problem is just as ill conditioned as (5). To find a particular solution, MCA follows a variational framework and minimizes a cost function chosen so as to promote sparsity

¹ In (6), matrix \mathbf{F}_i is usually considered an inverse transform, because it maps a set of coefficients in the transform domain to a signal. The notation here emphasizes the use of the transform to represent (synthesize) the sought component signals.

of \mathbf{a}_i . Once the optimal coefficients \mathbf{a}_1^* and \mathbf{a}_2^* are obtained, MCA then estimates the components \mathbf{x}_i as follows:

$$\hat{\mathbf{x}}_1 = \mathbf{F}_1 \mathbf{a}_1^*, \quad \hat{\mathbf{x}}_2 = \mathbf{F}_2 \mathbf{a}_2^*. \quad (8)$$

We assume that the columns of \mathbf{F}_1 and \mathbf{F}_2 form Parseval frames [16], i.e.,

$$\mathbf{F}_1 \mathbf{F}_1^H = \mathbf{I}, \quad \mathbf{F}_2 \mathbf{F}_2^H = \mathbf{I}, \quad (9)$$

where \mathbf{F}^H denotes the complex conjugate transpose of \mathbf{F} . Many classic transforms for digital signal processing, such as the discrete Fourier transform (DFT), discrete cosine transform, modified discrete cosine transform, and orthonormal wavelet transforms, satisfy (9). Numerous overcomplete transforms—the STFT [17], the steerable pyramid [18], and others [19]—satisfy (9) as well. An overcomplete transform is one that represents a signal of length N samples by a set of M coefficients with $M > N$. Hence, it is represented by a “wide” matrix \mathbf{F} of size $N \times M$; i.e., \mathbf{F} is neither square nor invertible. In this article, we use unitary and overcomplete transforms satisfying (9), because (9) simplifies the subsequent sparse optimization by which MCA is implemented.

INAPPLICABILITY OF LEAST SQUARES

To find optimal coefficients \mathbf{a}_i^* satisfying (7), one may consider a least squares (LS) approach. The LS approach may be formulated as

$$\{\mathbf{a}_1^*, \mathbf{a}_2^*\} = \arg \min_{\mathbf{a}_1, \mathbf{a}_2} \lambda_1 \|\mathbf{a}_1\|_2^2 + \lambda_2 \|\mathbf{a}_2\|_2^2 \quad (10a)$$

$$\text{such that } \mathbf{x} = \mathbf{F}_1 \mathbf{a}_1 + \mathbf{F}_2 \mathbf{a}_2, \quad (10b)$$

where $\|\mathbf{v}\|_2^2$ denotes the energy of $\mathbf{v} \in \mathbb{C}^N$; i.e., $\|\mathbf{v}\|_2^2 = \sum_n |\mathbf{v}(n)|^2$.

The solution to the LS problem in (10) can be found explicitly and is given by

$$\mathbf{b} = \left[\frac{1}{\lambda_1} \mathbf{F}_1 \mathbf{F}_1^H + \frac{1}{\lambda_2} \mathbf{F}_2 \mathbf{F}_2^H \right]^{-1} \mathbf{x}, \quad (11a)$$

$$\mathbf{a}_1^* = \frac{1}{\lambda_1} \mathbf{F}_1^H \mathbf{b}, \quad (11b)$$

$$\mathbf{a}_2^* = \frac{1}{\lambda_2} \mathbf{F}_2^H \mathbf{b}, \quad (11c)$$

where \mathbf{b} is a vector of Lagrange multipliers. Assuming the transforms \mathbf{F}_i satisfy (9), the LS solution in (11) can be written in a simplified form:

$$\mathbf{a}_1^* = \frac{1}{\lambda_1 \left(\frac{1}{\lambda_1} + \frac{1}{\lambda_2} \right)^{-1}} \mathbf{F}_1^H \mathbf{x} \quad (12a)$$

$$\mathbf{a}_2^* = \frac{1}{\lambda_2 \left(\frac{1}{\lambda_1} + \frac{1}{\lambda_2} \right)^{-1}} \mathbf{F}_2^H \mathbf{x} \quad (12b)$$

Hence, the LS-optimal components $\hat{\mathbf{x}}_i$, according to (8), are given by

$$\hat{\mathbf{x}}_1 = \frac{1}{\lambda_1 \left(\frac{1}{\lambda_1} + \frac{1}{\lambda_2} \right)^{-1}} \mathbf{x} \quad (13a)$$

$$\hat{\mathbf{x}}_2 = \frac{1}{\lambda_2 \left(\frac{1}{\lambda_1} + \frac{1}{\lambda_2} \right)^{-1}} \mathbf{x} \quad (13b)$$

However, these estimated component signal $\hat{\mathbf{x}}_i$ are only scaled versions of \mathbf{x} . That is, $\hat{\mathbf{x}}_1$ and $\hat{\mathbf{x}}_2$ both have the same shape as \mathbf{x} . They are only different from each other by a scaling factor. Specifically, the LS solution has the property

$$\hat{\mathbf{x}}_2 = \frac{\lambda_1}{\lambda_2} \hat{\mathbf{x}}_1. \quad (14)$$

In particular, no useful signal decomposition is accomplished using the LS formulation given in (10).

SPARSE OPTIMIZATION

Similar to the LS approach, one may consider an L1-norm minimization approach to find the optimal coefficients \mathbf{a}_i^* satisfying (7). The L1-norm approach may be formulated as

$$\{\mathbf{a}_1^*, \mathbf{a}_2^*\} = \arg \min_{\mathbf{a}_1, \mathbf{a}_2} \lambda_1 \|\mathbf{a}_1\|_1 + \lambda_2 \|\mathbf{a}_2\|_1 \quad (15a)$$

$$\text{such that } \mathbf{x} = \mathbf{F}_1 \mathbf{a}_1 + \mathbf{F}_2 \mathbf{a}_2, \quad (15b)$$

where $\|\mathbf{v}\|_1$ denotes the L1 norm of $\mathbf{v} \in \mathbb{C}^N$; i.e., $\|\mathbf{v}\|_1 = \sum_n |\mathbf{v}(n)|$.

In contrast to the LS approach, the L1-norm approach in (15) is frequently effective for signal decomposition, as demonstrated in the examples in the Experiments section later in this article and in the MCA literature [9], [20]. The minimization of the L1 norm corresponds to the prior knowledge that the distribution of coefficients \mathbf{a}_i is non-Gaussian; in particular, they have “fatter” tails and more mass around zero in comparison with the Gaussian distribution.

The MCA concept, i.e., modeling a signal as the sum components that are efficiently (sparsely) represented in distinct domains, originated in image processing [21], [22], especially for the problem of separating spatially overlapping texture and geometry [23], [24], [25]. These techniques have also been used for audio [26], speech [27], and radar [10].

The solution to the L1-norm minimization problem in (15) cannot be obtained by solving a system of linear equations.

That is, the L1-norm approach necessarily produces estimates $\hat{\mathbf{x}}_i$ that are nonlinear functions of \mathbf{x} . It may be said that the L1-norm minimization provides a principled approach to nonlinear signal separation. However, the L1-norm cost function in (15) is nondifferentiable (because the absolute value function is not differentiable at zero). Hence, the solution to (15) can be obtained only by iterative algorithms.

In addition, the nonsmooth problem in (15) is a large-scale problem: the number of optimization variables is at least $2N$, where N is the length of the signal \mathbf{x} . In this article, because we use the STFT with 50% overlapping (which is two times overcomplete) as one of the two transforms, there are $3N$ optimization variables.

For the sparse optimization approach in (15) to be useful in real-time applications, including radar, a fast algorithm must be available to compute its solution. Large-scale, nonsmooth optimization problems are typically difficult to solve quickly and reliably. Fortunately, fast matrix-free algorithms are available to minimize L1-norm functions with guaranteed global convergence properties, e.g., [28], [29], [30]. The minimization of L1-norm cost functions, such as in (15), is a key computational problem in sparsity-based methods in signal processing and statistics, and the development of fast, robust algorithms to solve such problems has been an active research area [31]. For general nonsmooth convex problems, algorithms based on proximity operators [32] have been developed [33], [34] that are applicable to a range of problems.

SPARSE SIGNAL SEPARATION WITH SPLIT AUGMENTED LAGRANGIAN SHRINKAGE ALGORITHM

A particularly effective (fast, globally convergent) algorithm for L1-norm signal separation in (15) is based on the split augmented Lagrangian shrinkage algorithm (SALSA) [35]. This algorithm is suitable for numerous ill-conditioned inverse problems arising in signal and image processing, particularly, when the LS form of the problem admits a fast solution (SALSA is based on solving a sequence of LS problems). An adaptation of SALSA leads to an efficient algorithm for MCA, particularly when the utilized transforms \mathbf{F}_i satisfy (9) [36]. SALSA, in turn, is based on the alternating direction method of multipliers (ADMM) [35], [37], which can be viewed as an application of the Douglas-Rachford algorithm [32], [38].

The first step of SALSA reformulates (15) by introducing auxiliary variables \mathbf{u}_1 and \mathbf{u}_2 :

$$\arg \min_{\mathbf{u}_1, \mathbf{u}_2} \lambda_1 \|\mathbf{u}_1\|_1 + \lambda_2 \|\mathbf{u}_2\|_1 \quad (16a)$$

$$\text{such that } \mathbf{F}_1 \mathbf{a}_1 + \mathbf{F}_2 \mathbf{a}_2 = \mathbf{x}, \quad (16b)$$

$$\mathbf{u}_1 - \mathbf{a}_1 = 0, \quad (16c)$$

$$\mathbf{u}_2 - \mathbf{a}_2 = 0. \quad (16d)$$

This reformulation leads subsequently to a decoupling between the L1-norm cost function and the constraint in (7). The next few steps of SALSA invoke the augmented Lagrangian and the ADMM to obtain the iterative algorithm:

Initialize: $\mu > 0$, \mathbf{d}_i , $i = 1, 2$

Repeat

$$\mathbf{u}_i = \arg \min_{\mathbf{u}_i} \lambda_i \|\mathbf{u}_i\|_1 + 0.5\mu \|\mathbf{u}_i - \mathbf{a}_i - \mathbf{d}_i\|_2^2, \quad i = 1, 2 \quad (17a)$$

$$\{\mathbf{a}_1, \mathbf{a}_2\} \begin{cases} \arg \min_{\mathbf{a}_1, \mathbf{a}_2} \|\mathbf{u}_1 - \mathbf{a}_1 - \mathbf{d}_1\|_2^2 + \|\mathbf{u}_2 - \mathbf{a}_2 - \mathbf{d}_2\|_2^2 \\ \text{such that } \mathbf{F}_1 \mathbf{a}_1 + \mathbf{F}_2 \mathbf{a}_2 = \mathbf{x} \end{cases} \quad (17b)$$

$$\mathbf{d}_i = \mathbf{d}_i - (\mathbf{u}_i - \mathbf{a}_i), \quad i = 1, 2 \quad (17c)$$

until convergence.

This algorithm alternates between minimizing with respect to \mathbf{u}_i and \mathbf{a}_i . The convergence of ADMM to the global optimal solution, in a general setting, is proven by Eckstein and Bertsekas [39]. The positive parameter μ is analogous to a step size parameter. The vectors \mathbf{d}_i are analogous to Lagrange multipliers. We initialize $\mathbf{d}_i = 0$, but the algorithm is globally convergent, regardless of the initialization.

The solution to the minimization subproblem in (17a) is given in closed form by $[\mathbf{u}_i]_n = \text{soft}([\mathbf{a}_i + \mathbf{d}_i]_n, \lambda/\mu)$, where soft is the soft-threshold function. In the complex plane, the function $\mathbb{C} \rightarrow \mathbb{C}$ is defined as

$$\text{soft}(y, T) = y \max(0, 1 - T/|y|), \quad y \in \mathbb{C}, T \in \mathbb{R}_+ \quad (18)$$

where T is the threshold value. This definition, when restricted to the real line, coincides with the usual soft-threshold function. The subproblem in (17b) is a constrained LS problem: the solution can be expressed explicitly in matrix form, which is further simplified using (9). With further simplifications [36], [40], the algorithm in (17) can be implemented as follows:

Initialize: $\mu > 0$, \mathbf{d}_i , $i = 1, 2$

Repeat

$$\mathbf{u}_i = \text{soft}(\mathbf{a}_i + \mathbf{d}_i, \lambda_i/\mu) - \mathbf{d}_i, \quad i = 1, 2 \quad (19a)$$

$$\mathbf{b} = \mathbf{x} - \mathbf{F}_1 \mathbf{u}_1 - \mathbf{F}_2 \mathbf{u}_2 \quad (19b)$$

$$\mathbf{d}_i = \frac{1}{2} \mathbf{F}_i^H \mathbf{b}, \quad i = 1, 2 \quad (19c)$$

$$\mathbf{a}_i = \mathbf{d}_i + \mathbf{u}_i, \quad i = 1, 2 \quad (19d)$$

until convergence.

Each iteration of the algorithm in (19) calls for soft-thresholding and forward and inverse transforms \mathbf{F}_i and \mathbf{F}_i^H . If the transforms admit fast implementations, then the algorithm in (19) is fast. Here, the optimization parameter μ dictate the convergence of the algorithm. The optimum values of λ_1 and λ_2 are data dependent and need to be selected based on the task at hand. In all examples discussed later in the Experiments section, we use the DFT and the STFT, both implemented using fast Fourier transforms (FFTs). For convenience, we also use a fixed number of 100 iterations of the algorithm, which we find sufficient for convergence. Because FFTs can be implemented efficiently, especially with parallel processors, and because a fixed number of iterations is effective, the algorithm in (19) can be used in applications requiring a fast, predictable run time.

ACCOUNTING FOR NOISE

Often, a noise component should be included in the signal model. In this case, the observed signal \mathbf{y} is written as

$$\mathbf{y} = \mathbf{x}_1 + \mathbf{x}_2 + \mathbf{w}, \quad (20)$$

where \mathbf{w} is white Gaussian noise. Sparse optimization can again be used to estimate the component signals \mathbf{x}_i when they admit sparse representations with respect to distinct transforms. To account for the presence of noise, the L1-norm approach may, in this case, be formulated as follows:

$$\{\mathbf{a}_1^*, \mathbf{a}_2^*\} = \arg \min_{\mathbf{a}_1, \mathbf{a}_2} \|\mathbf{y} - \mathbf{F}_1 \mathbf{a}_1 - \mathbf{F}_2 \mathbf{a}_2\|_2^2 + \lambda_1 \|\mathbf{a}_1\|_1 + \lambda_2 \|\mathbf{a}_2\|_1. \quad (21)$$

The use of the L1 norm to penalize a LS data fidelity term is sometimes called basis pursuit denoising [41] or the least absolute shrinkage and selection operator [42]. Fast algorithms, as discussed earlier, including a SALSA-like algorithm such as in (19), are also available for (21).

TRANSFORMS FOR SPARSE SIGNAL MODELING

For the experiments performed, we use the inverse DFT and the inverse STFT as transforms \mathbf{F}_1 and \mathbf{F}_2 , respectively. The DFT may be implemented with or without zero padding; hence, \mathbf{F}_1 may be either a wide or a square matrix, respectively. In the examples, the STFT is always implemented with 50% overlapping; hence, \mathbf{F}_2 is twice as wide as it is tall. The nonlinear separation algorithm in (19) depends on the transforms satisfying (9), which our DFT and STFT implementations satisfy in each example. The implementation of the STFT, so as to satisfy (9), is described in [17].

According to the first simulation discussed in the Experiments section, the DFT can be used to sparsely represent the radar returns $s_{\text{tar}}(t)$ generated by constant-velocity targets. Likewise, the STFT can be used to sparsely represent the returns $s_{\text{wtc}}(t)$ generated by wind turbines, because the STFT is suitable for the representation of time-varying Doppler char-

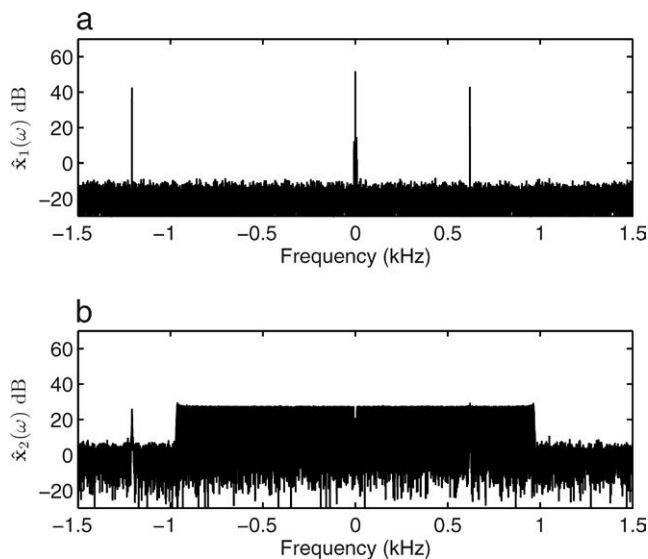


Figure 4. (a) Frequency spectrum of estimated component $\hat{s}_{tar}(\omega)$, including targets and stationary ground clutter. (b) Frequency spectrum of estimated component $\hat{s}_{wtc}(\omega)$, including wind turbine clutter and target-clutter residuals.

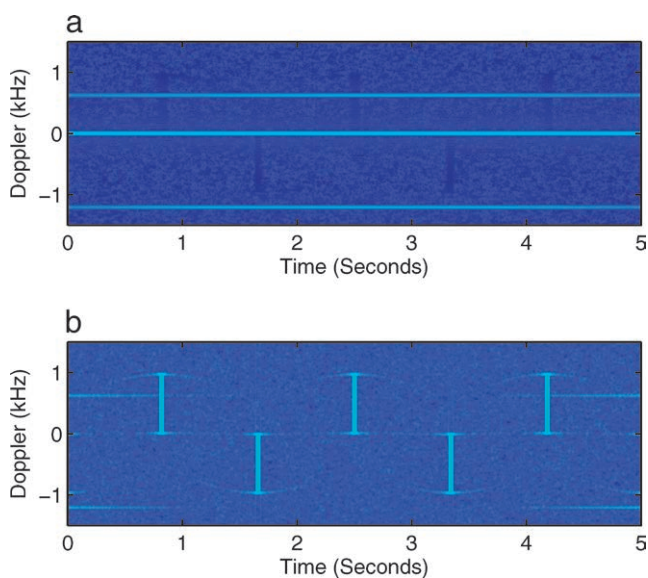


Figure 5. (a) Spectrogram of estimated component $\hat{s}_{tar}(t)$ comprises targets and stationary ground clutter. (b) Spectrogram of estimated component $\hat{s}_{wtc}(t)$ comprises wind turbine clutter and residual target-clutter.

acteristics. Even if the coefficients \mathbf{a}_i^* , optimized according to (15), are not sparse in an ideal sense, the L1-norm methodology achieves a degree of useful separation because of the relative sparsity of the component signals \mathbf{x}_i with respect to each of the transforms \mathbf{F}_i . (That is, \mathbf{s}_{tar} is sparser with respect to the DFT than with respect to the STFT, and \mathbf{s}_{wtc} is sparser with respect to the STFT than with respect to the DFT.)

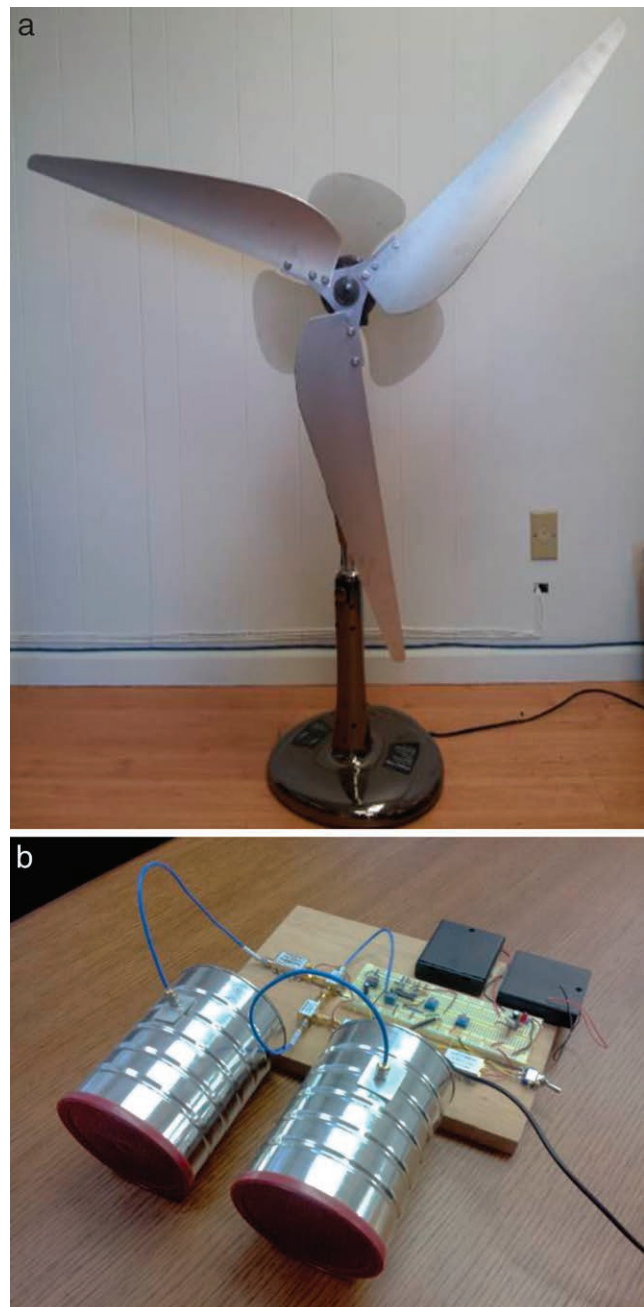


Figure 6. Customized fan (wind turbine proxy) and radar used for experiment.

EXPERIMENTS

In the following examples, the effectiveness of nonlinear L1-norm signal separation for the purpose of wind turbine clutter mitigation is demonstrated. The examples comprise (1) simulations; (2) radar data collected in house, wherein a customized fan (with turbinelike blades) serves as a stand-in for a wind turbine; and (3) wind turbine radar data provided by the U.S. Air Force Research Laboratory (AFRL).

SIMULATED ROTATING BLADE

We consider the simulated radar data $s(t)$ described earlier and illustrated in Figures 2c and 3b. We use the algorithm in (19) to decompose the total signal, $s(t)$ in (4), into a component signal due to targets $s_{\text{tar}}(t)$ and a component signal due to the wind turbine $s_{\text{wtc}}(t)$. The estimated signal components $\hat{s}_{\text{tar}}(t)$ and $\hat{s}_{\text{wtc}}(t)$ are obtained using 100 iterations of the algorithm in (19), at which point the algorithm was found to have converged. In this simulation, we used $\lambda_1 = 0.8$, $\lambda_2 = 0.2$, and $\mu = 0.5$.

The frequency spectra $\hat{S}_{\text{tar}}(\omega)$ and $\hat{S}_{\text{wtc}}(\omega)$ of the estimated signal components are illustrated in Figure 4. Observe in Figure 4a that $\hat{S}_{\text{tar}}(\omega)$ comprises moving targets, ground clutter, and stationary noise. However, as shown in Figure 4b, $\hat{S}_{\text{wtc}}(\omega)$ comprises wind turbine clutter (distinguished by its time-varying Doppler characteristics), a fraction of the target energy, and stationary noise. This noise arises in both estimated signals because we have used (19) rather than (21). In this simulation, we have set the parameter λ so that the estimated target signal component s_{tar} contains negligible observable wind turbine clutter. Depending on the selected λ value, there may be more or less leakage between the two estimated components signals; i.e., a fraction of $\hat{s}_{\text{tar}}(t)$ may be visible in $\hat{s}_{\text{wtc}}(t)$, or vice versa.

To further illustrate the simulation result, the spectrograms of the estimated component signals $\hat{s}_{\text{tar}}(t)$ and $\hat{s}_{\text{wtc}}(t)$ are shown in Figure 5. In Figure 5a, the wind turbine clutter has been effectively suppressed and the moving targets and ground clutter are clearly visible. There is no residual simulated wind turbine clutter in Figure 5a. As a final step, the ground clutter component can be suppressed using traditional band-pass filtering, Doppler filtering, or adaptive Doppler filtering.

EXPERIMENTAL RADAR

To complement the simulation, an experiment was conducted at C&P Technologies using an in-house S-band frequency-modulated continuous wave Doppler radar centered at

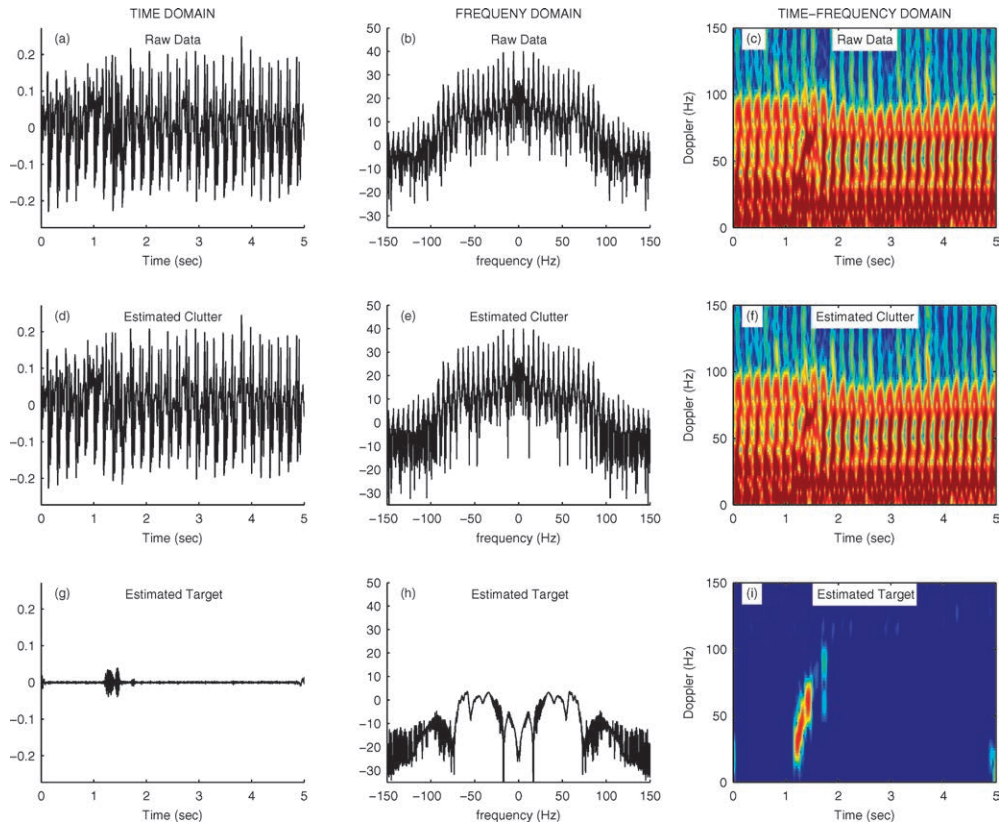


Figure 7.

Separation of signal components that overlap in time, frequency, and time-frequency. The acquired radar data comprise returns produced by a rotating blade and an accelerating object. (a), (d), and (g) Raw acquired radar data $s(t)$ and components $\hat{s}_{\text{wtc}}(t)$ and $\hat{s}_{\text{tar}}(t)$. (b), (e), and (h) Frequency spectra of the data and components signals. (c), (f), and (i) Spectrograms of the data and component signals. The separation is achieved based on distinct time-varying Doppler signatures.

2.4 GHz with 10 mW of power, similar to that described in [43], [44]. We used a large customized fan with three blades as a proxy for a wind turbine, as shown in Figure 6. Its distance to the radar was adjusted appropriately so that it presented a large surface area.

The radar unit is powered by a 5-V battery supply and is connected via an audio cable to a computer running MATLAB. The computer samples the output of the Doppler radar using its sound card at a sampling rate of 96 k samples/s. A 15-kHz antialiasing low-pass filter is installed between the radar and the computer. Single- and multiblade experiments have been conducted using the fan as a stand in for a wind turbine.

To evaluate the MCA approach for interference mitigation, a flying metal object was employed as a moving target in the presence of the rotating blade (fan). Figures 7a–7c show the acquired radar data time series $s(t)$, its frequency spectrum $S(\omega)$, and its spectrogram $S(t, \omega)$. (A 40-dB dynamic range is used for displaying the spectrograms.) Figure 7 shows that the signatures of the target and fan overlap in the time domain, in the frequency domain, and in the time-frequency domain. Conventional frequency-filtering techniques are ineffective for the separation of the fan and target,

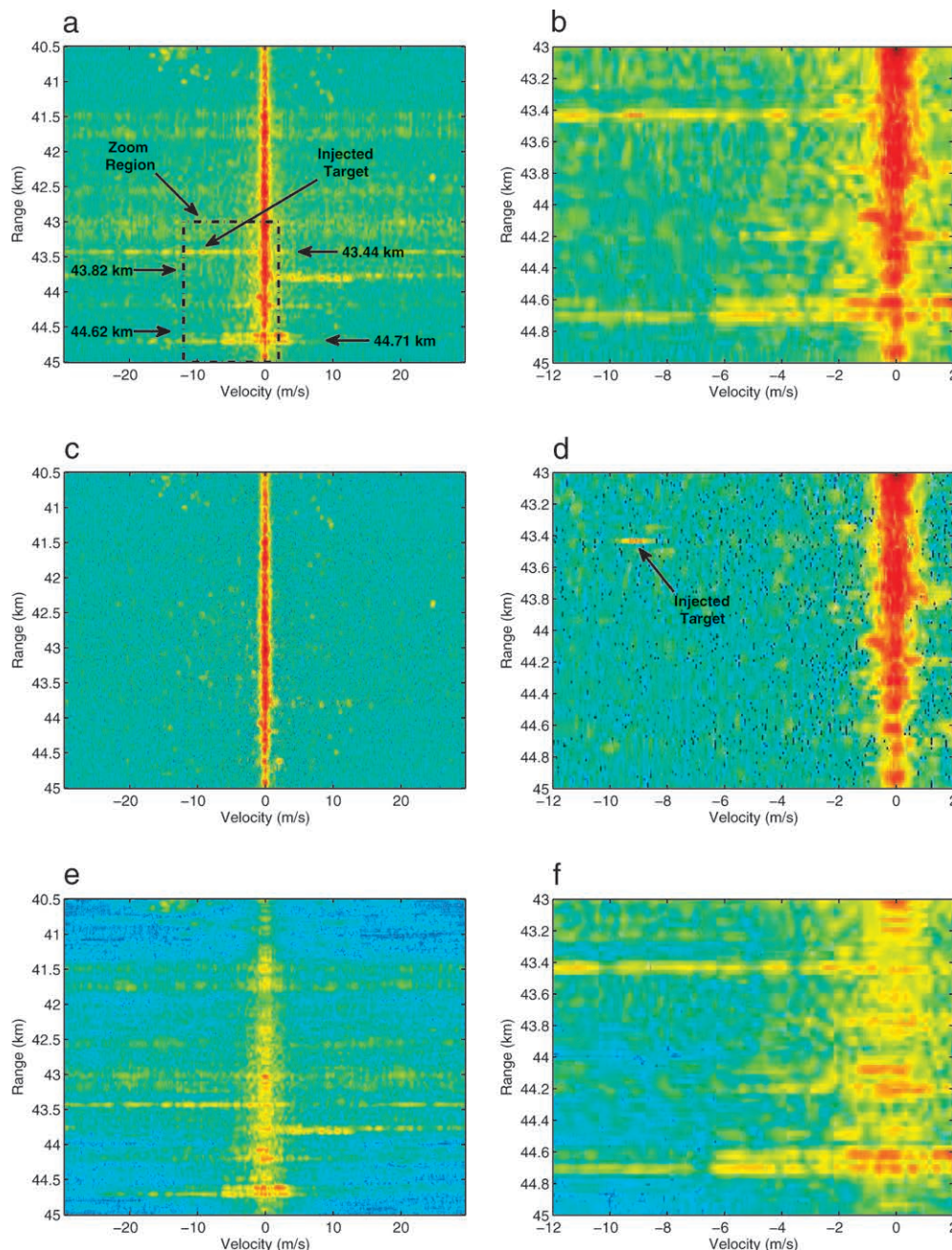


Figure 8.
Real radar data containing wind turbine clutter provided by the AFRL.

because the target is mostly buried within the return due to the fan.

We applied the algorithm in (19) to the radar data $s(t)$. For transform F_1 , we used the DFT with no zero padding; for transform F_2 , we used the STFT with a frame length of 256 samples and 50% overlapping. We set $\lambda_1 = 0.3$, $\lambda_2 = 0.7$, and $\mu = 10$. The algorithm was run for 100 iterations, at which point the algorithm was found to have converged. The estimated component signals $\hat{s}_{wtc}(t)$ and $\hat{s}_{tar}(t)$ are obtained using the DFT and STFT, respectively. Figures 7d–7f show $\hat{s}_{wtc}(t)$, and Figures 7g–7i show $\hat{s}_{tar}(t)$. As illustrated, the algorithm is able to achieve reasonable separation of the accelerating ob-

ject from the fan clutter. Interestingly, any thresholding operation in the time, frequency, or STFT domains is unable to separate the target from the clutter.

In the in-house experiment, the target component is estimated using the STFT, whereas in the simulation of the rotating blade discussed previously, the target component was estimated using the DFT. Thus, the roles of FFT and STFT are reversed in the experimental data set, and it follows that the model in (3) also reverses the roles of the two transforms. This is understandable because by design, the target was accelerating and consisted of only a short burst, whereas the single wind turbine model was rotating with a constant velocity. Nevertheless, the experiment is supportive of the notion that components with distinct time-varying Doppler spectra signatures can, in many cases, be separated using the MCA approach in (15), as implemented by the algorithm in (19).

WIND FARM CLUTTER

Figure 8 shows radar data containing wind turbine clutter provided by the AFRL (Wright-Patterson Air Force Base, Dayton, OH). For this analysis, we set $\lambda_1 = 0.45$, $\lambda_2 = 0.55$, and $\mu = 0.05$. For F_1 , we used the DFT; for transform

F_2 , we used the STFT with a frame length of 16 samples and 50% overlapping. The algorithm was run for 100 iterations, at which point the algorithm was found to have converged.

The area of detail is outlined with dashed lines in Figure 8a. In the figure, the locations of known wind turbines, and their distances from the radar, are indicated. Figures 8b, 8d, and 8f show the area of detail of Figures 8a, 8c, and 8e, respectively. As seen in Figure 8b, returns from the wind turbines result in Doppler streaking. These streaks have the potential to obscure moving targets. The success of the mitigation of wind turbine clutter is shown in Figure 8d. To simulate a

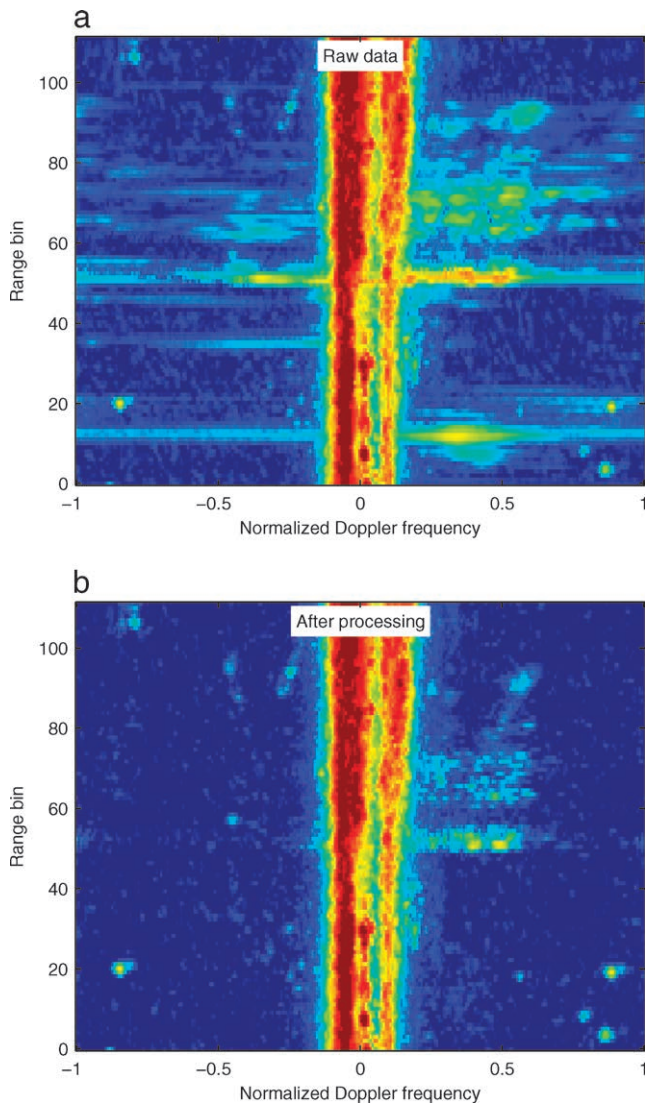


Figure 9. Range-Doppler profile formed using raw IQ data and IQ data preprocessed with nonlinear signal separation to suppress Doppler streaking.

target masking scenario, a moving target ($v_{\text{tar}} = 9$ m/s) was injected at a distance of 43.44 km from the receiver, where its Doppler signature exactly overlaps with the dynamic wind turbine clutter (Figure 8a and 8b). Figure 8b shows the area of detail of the injected target region. The Doppler streaking because of the wind turbine obscures the detection of the injected target. The success of the proposed algorithm under this scenario can be seen in Figure 8d, where the target is clearly visible, in contrast to Figure 8b.

OTHER APPLICATIONS

In addition to the wind turbine clutter mitigation, the proposed method may be useful to mitigate other types of dynamic clutter. One such application is illustrated next in the context of over-the-horizon radar (OTHR).

OVER-THE-HORIZON RADAR

This section considers the problem of suppressing Doppler-streak artifacts arising in range-Doppler profile images when strong transient interferences are present. An example of Doppler streaking, when conventional Doppler processing is used, is shown in Figure 9a. These data were acquired from an OTHR system. These Doppler streaks hinder the utility of the range-Doppler profile and may obscure moving targets of interest. This section demonstrates that MCA can be used as a preprocessing step to attenuate Doppler streaks [10]. The method consists first of using MCA to decompose the IQ data for each range bin into the sum of a two components: component $s_1(t)$ is modeled as sparse with respect to the STFT, and component $s_2(t)$ is modeled as sparse with respect to the FFT. After the decomposition is performed using the sparse optimization algorithm in (19), the range-Doppler profile is generated using component $s_2(t)$ by conventional Doppler processing. Using this technique on the IQ data of each range bin, we obtain the range-Doppler profile shown in Figure 9b, in which the streaking artifacts are substantially attenuated.

To clarify the cause of the Doppler streaking and to illustrate the role of MCA, it is informative to inspect the IQ data for one of the range bins. Range bin 52 in Figure 9a exhibits a fair degree of Doppler streaking. The complex IQ data $s(t)$, corresponding to this range bin, is shown in Figure 10a (only the real part is shown). It can be seen that $s(t)$ exhibits a fairly nonstationary behavior. During the first half of the dwell, $s(t)$ is essentially a single low-frequency component, perhaps because of stationary clutter. In the second half of the dwell, $s(t)$ also consists of higher-frequency energy, part of which is bursty. The nonstationary behavior leads to the Doppler-streak artifact.

Figures 10c and 10e show the optimized component signals $s_1(t)$ and $s_2(t)$, respectively. The components satisfy the constraint, $s(t) = s_1(t) + s_2(t)$. The component $s_1(t)$ comprises the most nonstationary characteristics of $s(t)$; it does not exhibit sustained oscillations but consists of brief pulses of energy at disparate frequencies. However, the component $s_2(t)$ is more nearly stationary. The decomposition of the IQ data can be further illustrated in the frequency domain. The spectra of $s(t)$ and of the component signals $s_1(t)$ and $s_2(t)$ are shown in Figures 10b, 10d, and 10f, respectively. The spectra of the two components overlap, yet the algorithm achieves an effective separation. This decomposition is achieved with minimal modeling; only the relative sparsity in two respective transform domains is assumed.

Using MCA in this way, nonstationary interference can be (partially) attenuated in the IQ data. Conventional Doppler processing (taper+FFT) can then be applied to the more stationary component. The result of applying this pre-Doppler processing procedure, as illustrated in Figure 9b, substantially reduces Doppler streaks, yet the procedure does not appear to adversely affect the features and potential targets of interest.

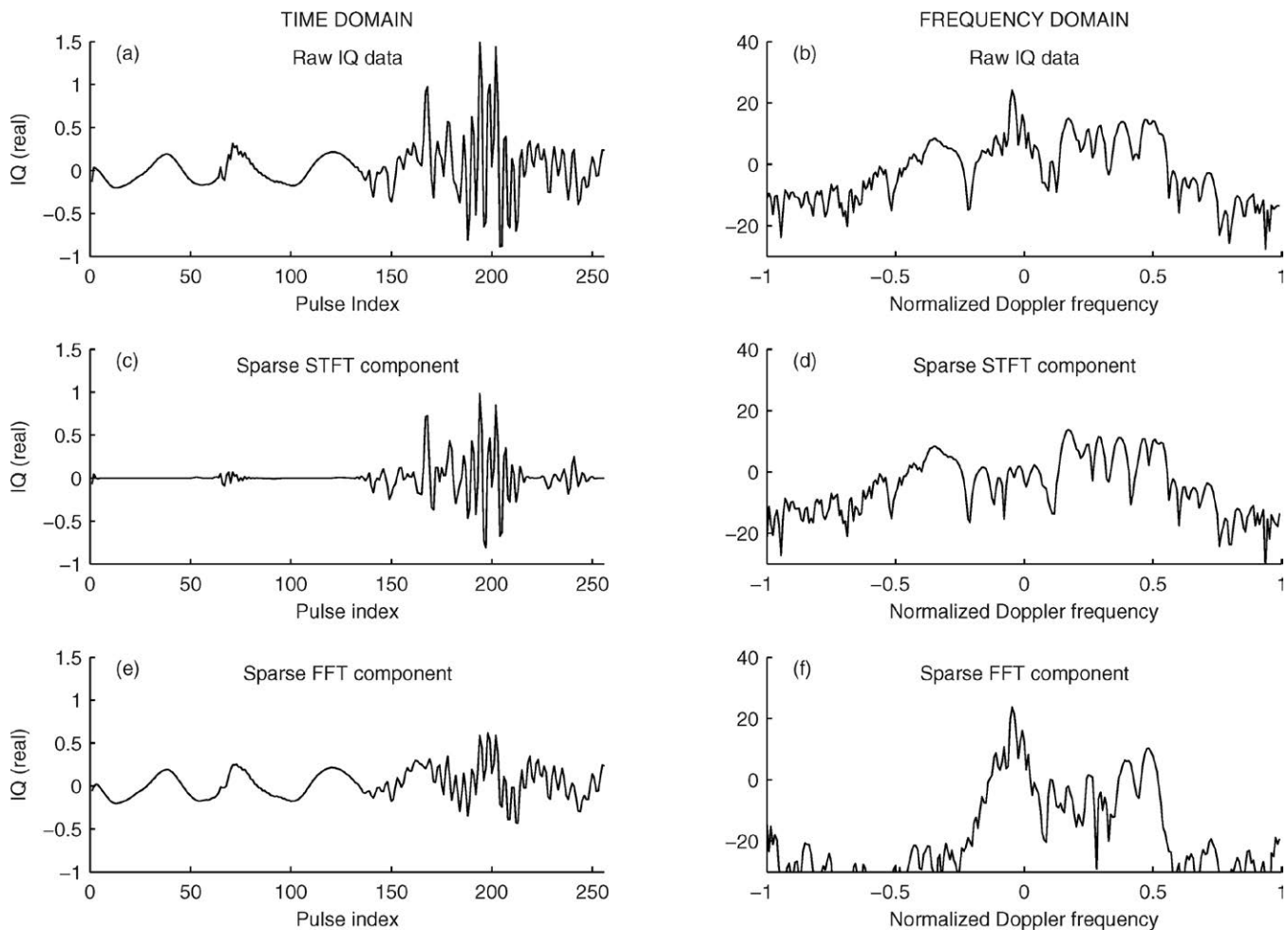


Figure 10.

(a) and (b) Raw IQ data $s(t)$ corresponding to range bin 52, and its Doppler spectrum. (c) and (d) Component $s_1(t)$ contains the more nonstationary behavior of $s(t)$. (e) and (f) Component $s_2(t)$ contains the more stationary behavior of $s(t)$. The components satisfy $s(t) = s_1(t) + s_2(t)$.

CONCLUSION

This article considers the problem of detecting moving targets buried in nontraditional wind turbine clutter using sparse optimization, specifically the MCA framework. Two transform domains—the FT and the STFT domains—are leveraged, wherein the constant-velocity targets and the wind turbine-like clutter, respectively, are (relatively) sparse. SALSA, adapted to MCA, is prescribed for solving the corresponding large-scale, nonsmooth L1-norm optimization problem.

We validate the approach using an experimental in-house system consisting of a custom-built radar and a customized fan. The results suggest that sparse optimization is a promising approach for separating radar return components by exploiting their time-varying Doppler characteristics. A numerical experiment is presented using a set of radar data exhibiting wind farm clutter. In addition, the method is applied to OTHR data for transient interference mitigation.

The L1-norm minimization approach shows promise as a methodology for addressing the detection of targets and challenging clutter. The minimization involves appropriate selection of certain optimization parameters. How to adaptively select them for a specific data set is an open question that requires further investigation. ♦

REFERENCES

- [1] American Wind Energy Association. Currently installed wind power capacity. AWEA, Washington, DC, 2012.
- [2] American Wind Energy Association. U.S. wind industry first quarter market report. AWEA, Washington, DC, Tech Rep., 2012.
- [3] Office of the Director of Defense Research and Engineering. The effect of windmill farms on military readiness. U.S. Department of Defense, Washington, DC, Tech Rep. ADA455993, 2006.
- [4] Hawk, S. Impact study of 130 offshore wind turbines in Nantucket sound. Tech Rep. AJW-W15B, Mar. 2009. <http://users>.

- ece.utexas.edu/~ling/US1%20Study_of_Nantucket_Wind_Farm_Report.pdf. Accessed June 8, 2014.
- [5] Butler, M. M., and Johnson, D. A. Feasibility of mitigating the effects of windfarms on primary radar. Alenia Marconi Systems, Tech Rep. W/14/00623/REP, June 2003. Available at http://users.ece.utexas.edu/~ling/EU1_Feasibility_Mitigating_Effects_Windfarms_on_Primary_Radar_Butler_Johnson_UK.pdf. Accessed June 8, 2014.
 - [6] Amato, N. J. Modeling and simulation architecture for studying Doppler-based radar with complex environments. Master's thesis, Air Force Institute of Technology, Wright-Patterson Air Force Base, Dayton, OH, Mar. 2009.
 - [7] Vogt, R. J., Reed, J. R., Crum, T., Snow, J. T., Palmer, R., Isom, B., et al. Impacts of wind farms on WSR-88D operations and policy considerations. In *Proceedings of the 23rd International Conference on Interactive Information Processing Systems (IIPS) for Meteorology, Oceanography, and Hydrology, American Meteorological Society, Preprints, Paper B*, Vol. 5, San Antonio, TX, 2007.
 - [8] Rashid, L., and Brown, A. Radar and wind farms. Presentation of the Microwave and Communication Systems Research Group, School of Electrical and Electronic Engineering at the University of Manchester, United Kingdom, 2010.
 - [9] Starck, J.-L., Moudden, Y., Bobina, J., Elad, M., and Donoho, D. Morphological component analysis. In *Proceedings of the SPIE (Wavelets XI)*, Vol. 5914, San Diego, CA, 2005.
 - [10] Selesnick, I. W., Li, K. Y., Pillai, S. U., and Himed, B. Doppler-streak attenuation via oscillatory-plus-transient decomposition of IQ data. In *Proceedings of the IET International Conference on Radar Systems*, Glasgow, United Kingdom, 2012.
 - [11] Chen, V. C., and Ling, H. *Time-Frequency Transforms for Radar Imaging and Signal Analysis*. Norwood, MA: Artech House, 2002.
 - [12] Chen, V. C. *The Micro-Doppler Effect in Radar*. Norwood, MA: Artech House, 2011.
 - [13] Naqvi, A., Yang, S.-T., and Ling, H. Investigation of Doppler features from wind turbine scattering. *IEEE Antennas and Wireless Propagation Letters*, Vol. 9 (2010), 485–488.
 - [14] Guerri, J. R. *Space-Time Adaptive Processing for Radar*. Norwood, MA: Artech House, 2003.
 - [15] Bobin, J., Starck, J.-L., Fadili, J. M., Moudden, Y., and Donoho, D. L. Morphological component analysis: an adaptive thresholding strategy. *IEEE Transactions on Image Processing*, Vol. 16, 11 (2007), 2675–2681.
 - [16] Kovačević, J., and Chebira, A. *An Introduction to Frames*. Hanover, MA: Now Publishers, 2008.
 - [17] Selesnick, I. The short-time Fourier transform and speech denoising. *Connexions*, 2009. [Online] <http://cnx.org/content/m32294>.
 - [18] Freeman, W. T., and Adelson, E. H. The design and use of steerable filters. *IEEE Transactions on Pattern Analysis and Machine Intelligence*, Vol. 13 (Sept. 1991), 891–906.
 - [19] Jacques, L., Duval, L., Chaux, C., and Peyré, G. A panorama on multiscale geometric representations, intertwining spatial, directional and frequency selectivity. *Signal Processing*, Vol. 91 (Dec. 2011), 2699–2730.
 - [20] Elad, M., Starck, J., Querre, P., and Donoho, D. Simultaneous cartoon and texture image inpainting using morphological component analysis (MCA). *Applied and Computational Harmonic Analysis*, Vol. 19 (Nov. 2005), 340–358.
 - [21] Aujol, J.-F., Aubert, G., Blanc-Féraud, L., and Chambolle, A. Image decomposition into a bounded variation component and an oscillating component. *Journal of Mathematical Imaging and Vision*, Vol. 22 (2005), 71–88.
 - [22] Vese, L. A., and Osher, S. Image denoising and decomposition with total variation minimization and oscillatory functions. *Journal of Mathematical Imaging and Vision*, Vol. 20 (2004), 7–18.
 - [23] Aujol, J.-F., Gilboa, G., Chan, T., and Osher, S. J. Structure–texture image decomposition: modeling, algorithms, and parameter selection. *International Journal of Computer Vision*, Vol. 67 (Apr. 2006), 111–136.
 - [24] Starck, J.-L., Elad, M., and Donoho, D. Image decomposition via the combination of sparse representation and a variational approach. *IEEE Transactions on Image Processing*, Vol. 14 (Oct. 2005), 1570–1582.
 - [25] Briceño-Arias, L. M., Combettes, P. L., Pesquet, J.-C., and Pustelnik, N. Proximal method for geometry and texture image decomposition. In *Proceedings of the IEEE International Conference on Image Processing*, Hong Kong, China, 2010, 2721–2724.
 - [26] Daudet, L., and Torrèsani, B. Hybrid representations for audio-phonetic signal encoding. *Signal Processing*, Vol. 82 (Nov. 2002), 1595–1617.
 - [27] Selesnick, I. W. Resonance-based signal decomposition: a new sparsity-enabled signal analysis method. *Signal Processing*, Vol. 91, 12 (2011), 2793–2809.
 - [28] Daubechies, I., Defrise, M., and De Mol, C. An iterative thresholding algorithm for linear inverse problems with a sparsity constraint. *Communications on Pure and Applied Mathematics*, Vol. 57, 11 (2004), 1413–1457.
 - [29] Bioucas-Dias, J., and Figueiredo, M. A new twist: two-step iterative shrinkage/thresholding algorithms for image restoration. *IEEE Transactions on Image Processing*, Vol. 16 (Dec. 2007), 2992–3004.
 - [30] Beck, A., and Teboulle, M. A fast iterative shrinkage-thresholding algorithm for linear inverse problems. *SIAM Journal on Imaging Sciences*, Vol. 2, 1 (2009), 183–202.
 - [31] Zibulevsky, M., and Elad, M. L1–L2 optimization in signal and image processing. *IEEE Signal Processing Magazine*, Vol. 27, 3 (2010), 76–88.
 - [32] Combettes, P. L., and Pesquet, J.-C. Proximal splitting methods in signal processing. In *Fixed-Point Algorithms for Inverse Problems in Science and Engineering*, H. H. Bauschke et al., Eds. New York: Springer-Verlag, 2011, pp. 185–212.
 - [33] Pesquet, J.-C., and Pustelnik, N. A parallel inertial proximal optimization method. *Pacific Journal of Optimization*, Vol. 8 (Apr. 2012), 273–305.
 - [34] Chambolle, A., and Pock, T. A first-order primal–dual algorithm for convex problems with applications to imaging. *Journal of Mathematical Imaging and Vision*, Vol. 40, 1 (2011), 120–145.
 - [35] Afonso, M. V., Bioucas-Dias, J. M., and Figueiredo, M. A. T. Fast image recovery using variable splitting and constrained opti-

- mization. *IEEE Transactions on Image Processing*, Vol. 19 (Sept. 2010), 2345–2356.
- [36] Selesnick, I. W. Sparse signal representations using the tunable Q-factor wavelet transform. In *Proceedings of the SPIE (Wavelets and Sparsity XIV)*, Vol. 8138, San Diego, CA, 2011.
 - [37] Boyd, S., Parikh, N., Chu, E., Peleato, B., and Eckstein, J. Distributed optimization and statistical learning via the alternating direction method of multipliers. *Foundations and Trends in Machine Learning*, Vol. 3, 1 (2011), 1–122.
 - [38] Raguet, H., Fadili, J., and Peyré, G. A generalized forward-backward splitting. *SIAM Journal on Imaging Sciences*, Vol. 6, 3 (2013), 1199–1226.
 - [39] Eckstein, J., and Bertsekas, D. On the Douglas-Rachford splitting method and the proximal point algorithm for maximal monotone operators. *Mathematical Programming*, Vol. 5 (1992), 293–318.
 - [40] Selesnick, I. L1-norm penalized least squares with SALSA. *Connections*, 2014. [Online] <http://cnx.org/content/m48933>.
 - [41] Chen, S., Donoho, D. L., and Saunders, M. A. Atomic decomposition by basis pursuit. *SIAM Journal on Scientific Computing*, Vol. 20 (1998), 33–61.
 - [42] Tibshirani, R. Regression shrinkage and selection via the lasso. *Journal of the Royal Statistical Society—Series B: Statistical Methodology B*, Vol. 58, 1 (1996), 267–288.
 - [43] Charvat, G., Fenn, A., and Perry, B. The MIT IAP radar course: build a small radar system capable of sensing range, Doppler, and synthetic aperture (SAR) imaging. In *Proceedings of the IEEE Radar Conference*, Atlanta, GA, 2012, 138–144.
 - [44] Uysal, F., Selesnick, I. W., Pillai, S. U., and Himed, B. Signal decomposition for wind turbine clutter mitigation. In *Proceedings of the IEEE Radar Conference*, Cincinnati, OH. (2014), to be published.